



HAL
open science

Observations of Quiescent Solar Wind Regions with Near-f ce Wave Activity

Benjamin Short, David M. Malaspina, Jasper Halekas, Orlando Romeo, J. L. Verniero, Adam J. Finley, Justin C. Kasper, Ali Rahmati, Stuart D. Bale, John W. Bonnell, et al.

► **To cite this version:**

Benjamin Short, David M. Malaspina, Jasper Halekas, Orlando Romeo, J. L. Verniero, et al.. Observations of Quiescent Solar Wind Regions with Near-f ce Wave Activity. *The Astrophysical Journal*, 2022, 940, 10.3847/1538-4357/ac97e4 . insu-04089884

HAL Id: insu-04089884

<https://insu.hal.science/insu-04089884>

Submitted on 5 May 2023

HAL is a multi-disciplinary open access archive for the deposit and dissemination of scientific research documents, whether they are published or not. The documents may come from teaching and research institutions in France or abroad, or from public or private research centers.

L'archive ouverte pluridisciplinaire **HAL**, est destinée au dépôt et à la diffusion de documents scientifiques de niveau recherche, publiés ou non, émanant des établissements d'enseignement et de recherche français ou étrangers, des laboratoires publics ou privés.



Distributed under a Creative Commons Attribution 4.0 International License



Observations of Quiescent Solar Wind Regions with Near- f_{ce} Wave Activity

Benjamin Short^{1,2}, David M. Malaspina^{2,3}, Jasper Halekas⁴, Orlando Romeo⁵, J. L. Verniero⁶, Adam J. Finley⁷, Justin C. Kasper⁸, Ali Rahmati⁵, Stuart D. Bale^{5,9}, John W. Bonnell⁵, Anthony W. Case¹⁰, Thierry Dudok de Wit¹¹, Keith Goetz¹², Katherine Goodrich¹³, Peter R. Harvey⁵, Kelly E. Korreck¹⁰, Davin Larson⁵, Roberto Livi⁵, Robert J. MacDowall⁶, Marc Pulupa⁵, Michael L. Stevens¹⁰, and Phyllis Whittlesey⁵

¹Department of Physics, University of Colorado, Boulder, CO, USA; Benjamin.Short@lasp.colorado.edu

²Laboratory for Atmospheric and Space Physics, University of Colorado, Boulder, CO, USA

³Astrophysical and Planetary Sciences Department, University of Colorado, Boulder, CO, USA

⁴University of Iowa, Iowa City, IA, USA

⁵Space Sciences Laboratory, University of California, Berkeley, CA, USA

⁶NASA Goddard Space Flight Center, Greenbelt, MD, USA

⁷Department of Astrophysics-AIM, University of Paris-Saclay and University of Paris, CEA, CNRS, Gif-sur-Yvette Cedex F-91191, France

⁸University of Michigan, Ann Arbor, MI, USA

⁹Physics Department, University of California, Berkeley, CA, USA

¹⁰Harvard-Smithsonian Center for Astrophysics, Cambridge, MA, USA

¹¹LPC2E, CNRS, and University of Orléans, Orléans, France

¹²School of Physics and Astronomy, University of Minnesota, Minneapolis, MN, USA

¹³Department of Physics and Astronomy, West Virginia University, Morgantown, WV, USA

Received 2022 June 8; revised 2022 October 3; accepted 2022 October 4; published 2022 November 18

Abstract

In situ measurements in the near-Sun solar wind from the Parker Solar Probe have revealed the existence of quiescent solar wind regions: extended regions of solar wind with low-amplitude turbulent magnetic field fluctuations compared to adjacent regions. Identified through the study of harmonic waves near the electron cyclotron frequency (f_{ce}), these quiescent regions are shown to host a variety of plasma waves. The near- f_{ce} harmonic waves are observed exclusively in quiescent regions, and as such, they can be used as markers for quiescent regions. A blob-finding algorithm is applied to data from Encounters 1–6 in order to identify near- f_{ce} harmonic wave intervals and thereby locate quiescent regions. We carry out a superposed epoch analysis on the identified quiescent regions, and compare their bulk solar wind properties with adjacent regions of solar wind. Quiescent regions are found to contain relatively weak magnetic field variation and are entirely devoid of magnetic switchbacks. In the quiescent solar wind, the magnetic field closely follows the Parker spiral, while adjacent regions prefer more radial orientations, providing a clear picture of the magnetic geometry of these regions. Quiescent regions show minimal differences in multiple particle plasma parameters relative to the non-quiescent solar wind. The quiescent solar wind regions, studied throughout this work, are thought to represent the underlying solar wind, through which Alfvénic fluctuations propagate. Quantifying the properties of these regions may help to understand the formation/origin of the solar wind, and furthermore, to constrain the role that low-frequency Alfvén waves play in the regulation of solar wind temperature.

Unified Astronomy Thesaurus concepts: [Solar wind \(1534\)](#); [Interplanetary turbulence \(830\)](#); [Space plasmas \(1544\)](#); [Solar magnetic fields \(1503\)](#); [Heliosphere \(711\)](#)

1. Introduction

In 2018 August, the Parker Solar Probe (PSP) launched with the purpose of studying the creation and evolution of the solar wind, the interplanetary magnetic field, and energetic particles found within, by approaching the Sun more closely than any other spacecraft to date. The previous records were held by Helios probes 1 and 2, which reached 0.31 au (~ 66.6 solar radii (R_s)) and 0.29 au (~ 62.4 R_s), respectively (Porsche 1981). On its first orbit, PSP reached a perihelion of 35.6 R_s , and since then it has descended down to 13.3 R_s . During PSP’s perihelion passes (referred to as encounters), PSP instruments detected regions of sharp Alfvénic fluctuations, termed switchbacks, interspersed between “quiet” regions of low turbulence in the radial component of the magnetic field (Bale et al. 2019;

Kasper et al. 2019; Dudok de Wit et al. 2020; Horbury et al. 2020). Switchbacks are characterized by reversals or sharp bends in the interplanetary magnetic field. Switchbacks are highly Alfvénic, pressure-balance structures, in that both the particle pressure and the magnetic pressure are constant across a switchback. As such, the magnetic field vector changes orientation but the magnitude of the magnetic field remains constant. At the time of writing, theories for the origins of the magnetic switchbacks fall into two main categories. The first is that switchbacks develop over time during the course of solar wind propagation. Schwadron & McComas (2021) present a version of this theory where switchbacks form as velocity shear contorts the magnetic field into an S-like geometry. Squire et al. (2020); Shoda et al. (2021) demonstrate that switchbacks can form naturally as a consequence of Alfvén wave turbulence, as the solar wind expands into the heliosphere, generating a bent field line as well as an accompanying bulk velocity perturbation. Conversely, in the second set of theories, switchbacks are formed by reconnection in the low corona, possibly at the edges of field loops and open field lines through a process

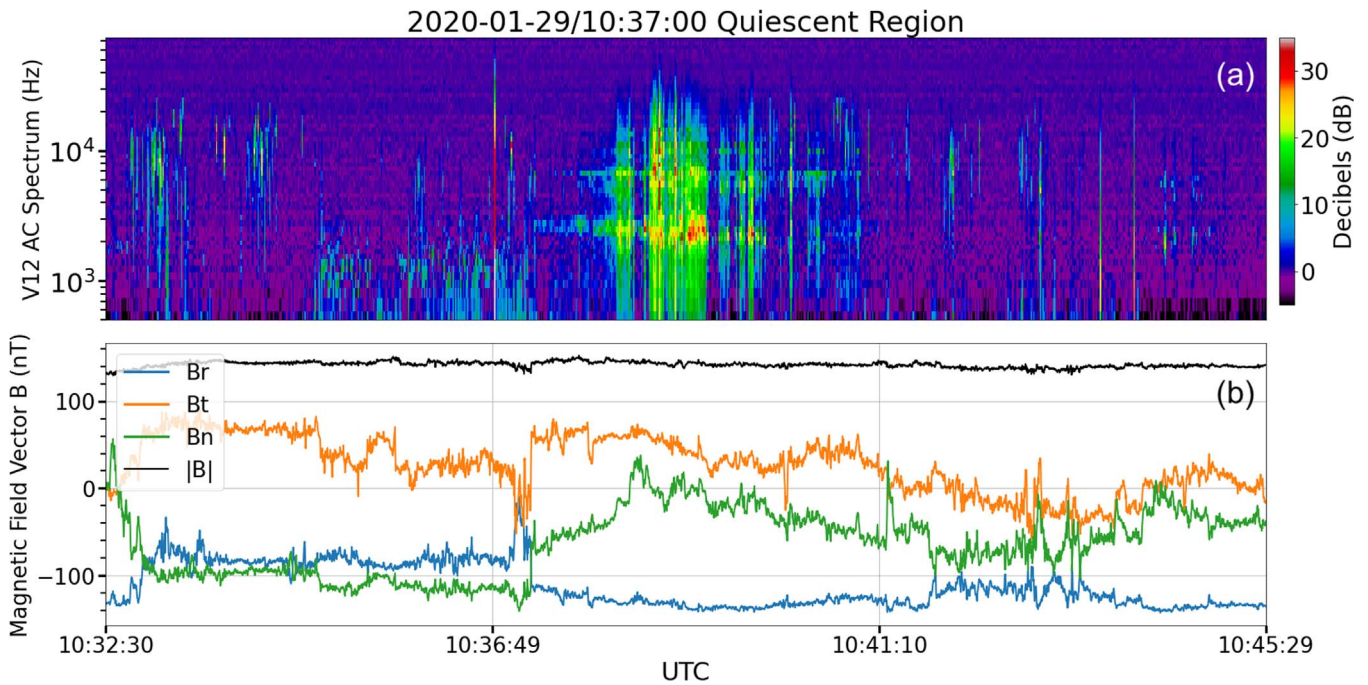


Figure 1. Example of a wave-active quiescent region. Figure 1(a) contains the V12 AC Spectrum of a wave-active quiescent region. Figure 1(b) is a plot of the magnetic field vector \vec{B} . It is observed that, during the interval with wave power, the magnetic field appears to take on particular characteristics. It has been shown that these intervals are associated with times of near-radial magnetic field with low levels of magnetic turbulence. It is these characteristics and their limits that this study seeks to explore.

called interchange reconnection (Axford et al. 1999; Bale et al. 2021; Drake et al. 2021). In the first view, the switchbacks are an effect of the differential wind speed rather than a cause of differential wind speeds. In the latter view, switchbacks form as low coronal structures interact and reconnect. Here, the switchback generation mechanism is independent of the relative velocities of the surrounding plasma, and leaves open the possibility that switchbacks play a role in solar wind acceleration and heating of the solar corona. Clusters of switchback magnetic fields are observed, potentially structured on the scale of supergranules on the solar surface (Bale et al. 2021; Fargette et al. 2021).

Interspersed between switchback patches in the solar wind are regions of low-turbulence, near-radial magnetic field termed “quiet” regions (Bale et al. 2019). Within these quiet regions are special regions with Parker spiral-like field geometries called “quiescent” regions (Dudok de Wit et al. 2020). These quiescent regions are characterized by both low-amplitude Alfvénic fluctuations and field geometries approaching that of a theoretical Parker spiral. These quiescent regions afford the ability to test theories of turbulent solar wind heating and acceleration by providing a strong contrast to the turbulent switchback patches. Dudok de Wit et al. (2020) demonstrated that the power spectral density of the magnetic fluctuations is very different in these regions compared to the average solar wind. Namely, the power spectra in the quiescent regions has spectral break points at frequencies more than an order of magnitude smaller than the rest of the solar wind. This could indicate that the quiescent regions are less turbulently evolved solar wind, possibly having undergone comparatively little evolution during propagation from the corona (Bruno & Carbone 2013; Matteini et al. 2018; Dudok de Wit et al. 2020). Because of their turbulent properties, these regions may be useful in constraining the role of turbulent stochastic heating in

the solar wind. In stochastic heating processes, an Alfvén wave that varies on ion gyroradius spatial scales will break the adiabatic orbital motion of those ions, enabling the transfer of energy in the direction perpendicular to the background magnetic field (Chandran et al. 2010).

The quiescent regions discussed in this study are a special subset of quiescent regions studied in Dudok de Wit et al. (2020). Malaspina et al. (2020) observed that this subset of quiescent regions are associated with times of intense electrostatic plasma wave activity, shown in Figure 1, and can be called “wave-active quiescent regions.” Like the larger set of quiescent regions, the ambient magnetic field is oriented largely along a Parker spiral during the times of wave activity (Malaspina et al. 2020). In this study, we use a larger data set to explore the properties of these wave-active quiescent regions. For simplicity, going forward we refer to these “wave-active quiescent regions” simply as “quiescent regions,” and proceed with the understanding that the regions discussed here overlap with but are not necessarily the same as the regions observed in Dudok de Wit et al. (2020).

2. Data Set and Processing

The Parker Solar Probe mission consists of 24 close approaches to the Sun. Using Venus gravity assists, these 24 orbits are split into eight orbit families, bringing the probe incrementally closer to the Sun. This study covers the first six orbits, including perihelion distances of 35.6 R_s , 27.8 R_s , and 20.3 R_s . This study utilizes data collected by the FIELDS instrument and by the Solar Wind Electrons Alphas and Protons (SWEAP) particle instruments on board PSP.

The FIELDS instrument (Bale et al. 2016) includes four 2 m antennas (V_1 , V_2 , V_3 , and V_4) positioned in the plane of the heat shield, one 21 cm antenna (V_5) positioned on a 3.5 m boom located on the rear of the spacecraft, two FGMs located on this

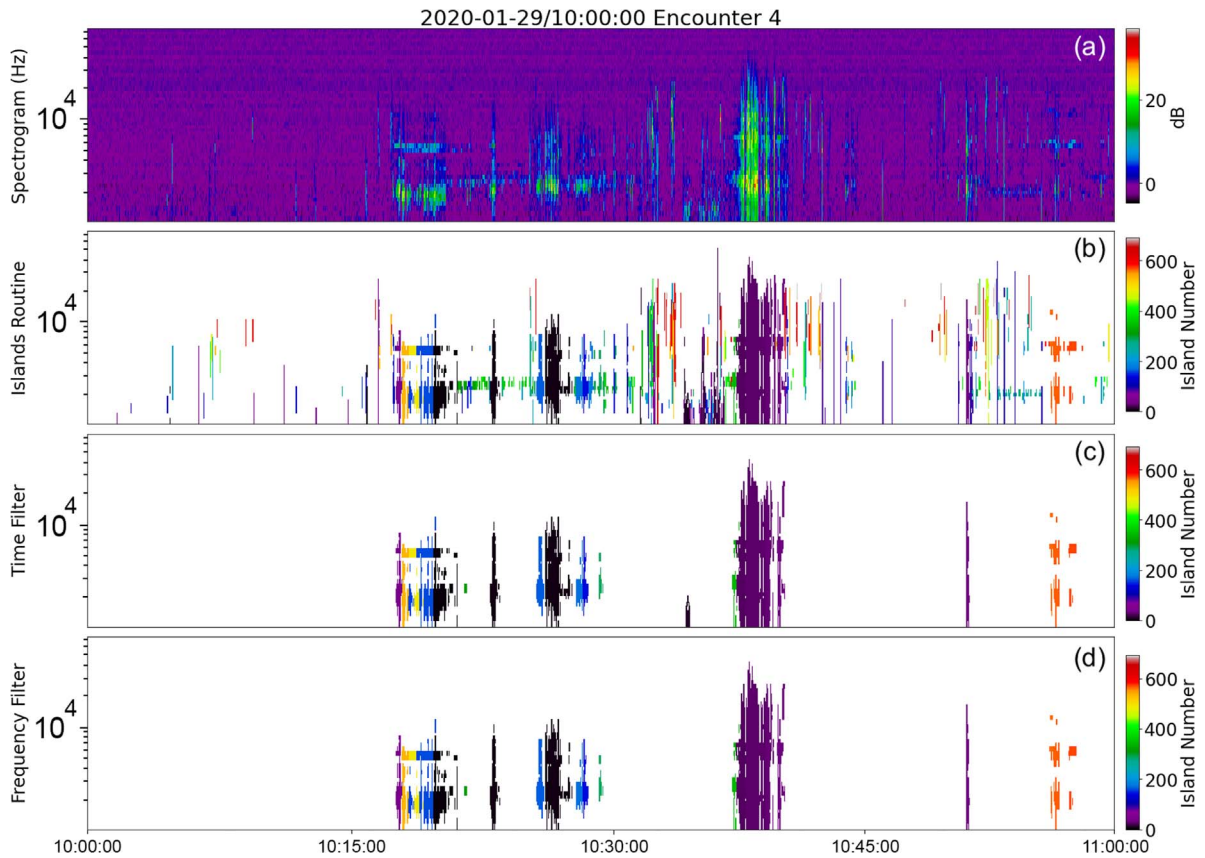


Figure 2. Demonstration of the wave-finding algorithm. Figure 2(a) shows the V12 AC spectrogram from 2020-01-29/10:00:00 to 2020-01-29/11:00:00 UTC. At roughly 10:40:00, there is significant wave power near f_{ce} . This set of wave power is an ideal example of the spectra we are looking for. Generally, there are two or more frequency bands that occur at the same time, roughly at 0.7 and $1 f_{ce}$. Figure 2(b) shows the output of the island-locating routine. Figure 2(c) shows the island output after a 7 s time filter is applied. Figure 2(d) shows the island output after the frequency threshold of $\geq 0.5 f_{ce}$ is applied. These limitations of wave frequency are discussed in Malaspina et al. (2020).

boom, and a search coil magnetometer (SCM) positioned at the end of the boom. Antenna pairs are located 180° apart, with the two pairs oriented 85° apart, 5° from perpendicular. Voltages from each antenna pair are used to create differential voltages: $V_{12} = V_1 - V_2$ and $V_{34} = V_3 - V_4$. Here, V_5 describes the voltage of the aft antenna and $V_z = V_5 - (V_1 + V_2 + V_3 + V_4)/4$. This study uses AC-coupled survey power spectra of the voltage measured by the V_{12} differential antenna pair. The AC power spectra, computed by the Digital Fields Board (DFB; Malaspina et al. 2016) cover a frequency range of 140 Hz to 75 kHz, with spectra output at a cadence of ~ 1.14 Sa/s. The study also uses magnetic field data collected by the fluxgate magnetometers (FGMs). These data are measured along three orthogonal axes at a cadence of 146.5 Sa/s and then rotated into spacecraft (SC) coordinates.

This study uses particle distributions and derivative quantities from the SWEAP instruments for electrons, protons, and alpha particles (Kasper et al. 2016; Livi et al. 2021). Using the SPAN-I moments, the ion temperatures, densities, bulk velocities, and temperature anisotropies are calculated. From SPAN-e (Whittlesey et al. 2020), distribution fits were determined following the fitting procedures used in Halekas et al. (2020) and are used to determine the electron temperature, temperature anisotropy, density, and core drift. The electron strahl widths are determined by a convolved Gaussian fit of the electron strahl population within the FOV of both SPAN-Ae and SPAN-Be. In figures involving Encounter 1, the Solar Probe Cup (SPC) instrument fits are used to find bulk velocity values, as SPAN-I was set to

the incorrect energy range for that encounter and could not measure the proton distribution as accurately.

For the purposes of this study, we are searching for individual events that are long-duration and contain waves of a particular frequency range to define quiescent regions. These events, once compiled, will be used to perform superposed epoch study of these quiescent regions. To that end, an algorithm is used to identify near- f_{ce} harmonic waves, which act as markers for these regions. The algorithm is as follows. The V_{12} AC-coupled power spectra are split into hour-long segments and their amplitudes (P_i) converted to decibels dB above the background noise (P_{0i}):

$$dB_i = 10 \log_{10}(P_i/P_{0i}),$$

where background noise is defined as the median in time,

$$P_{0i} = \text{Median}(P_i),$$

for P_i across a 24 hr window, for each frequency bin i .

An island-locating routine is then applied to the data. This routine converts the spectrogram “image” into “islands” and “oceans” where an island is any power value above 4 dB (assigned a label “1”). Oceans are assigned a label “0”. This threshold value was chosen because typical peak powers for these near- f_{ce} are in the 20–35 dB range, and 4 dB readily distinguishes these waves from background.

The algorithm then acts on this converted matrix of pixels (with distinguishing labels “1” and “0”), grouping pixels labeled with a “1” that are directly connected, in a side-by-

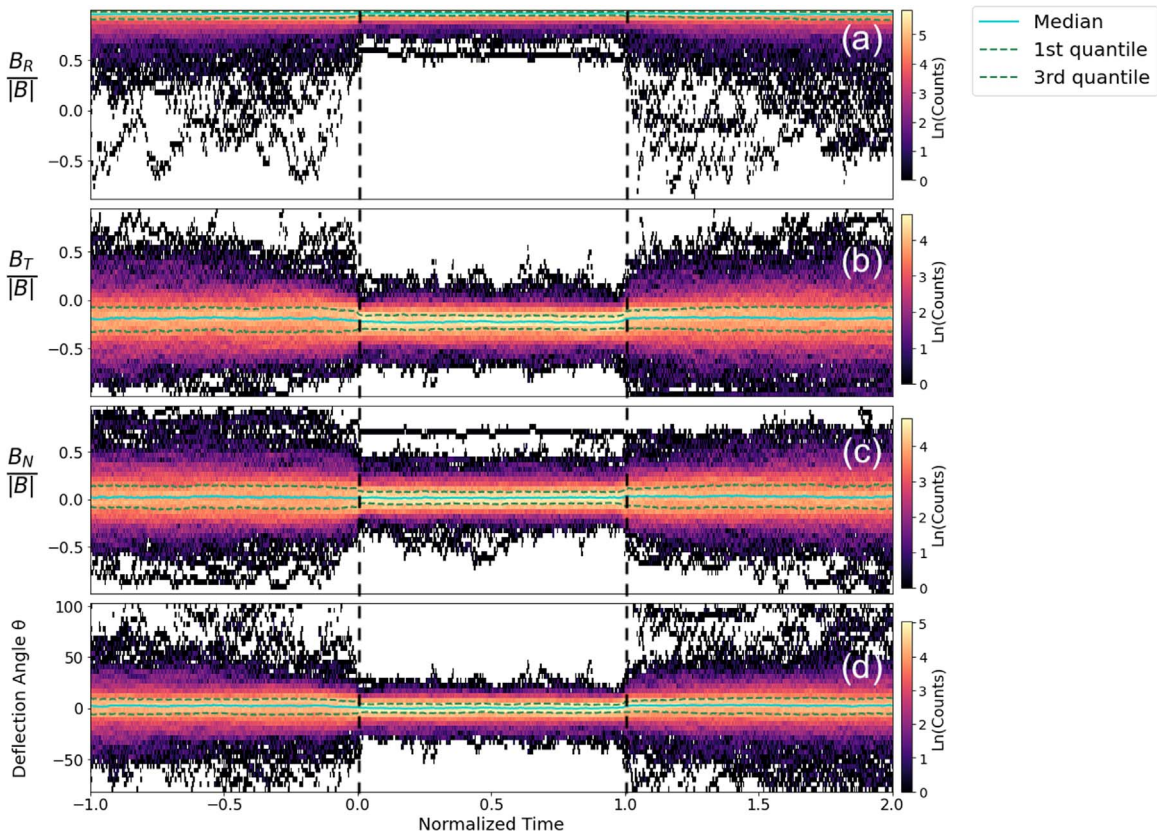


Figure 3. 2D histograms of magnetic field unit vectors and deflection angle from a nominal Parker spiral. Figure 3(a) shows the R component of the magnetic field unit vector in RTN coordinates. 3(b) shows the T component. 3(c) shows the N component. Figure 3(d) shows the angle that the magnetic field unit vector makes with respect to a theoretical Parker spiral. Counts are given in log scale to highlight changes in variance. SPC velocity values are used to calculate the Parker spiral for Encounter 1.

side manner (in both frequency and time dimensions), with neighboring “1” pixels into what we will soon call our quiescent regions. Each of the resulting groups is assigned a numerical index. Once all regions are indexed, the start time and time duration of each region are recorded, and regions less than 7 s long are removed from the quiescent region list. This cutoff is chosen because the wave events targeted by this study include the longest-lasting wave events that appear during Encounters 1 through 6. Choosing a time window greater than 7 s also removed dust impacts, ion acoustic waves (Mozer et al. 2020), and other short-lived events that appear in the AC spectral data.

Next, a frequency filter is applied using the median frequency of the power spectral data in each identified region. Any region with a median frequency that is less than half the local f_{ce} is removed. This reduces the amount of low-frequency wave power and noise that sometimes appear during certain intervals during encounters. This frequency threshold has also been shown to be an appropriate lower bound for the specific waves targeted in this study (Malaspina et al. 2020). Once these filters are applied, a list of the waves’ start times and their durations in s is generated.

The events on this list were then further examined by eye and marked with a 1 if a wave was determined to be a near- f_{ce} harmonic wave, and 0 otherwise.

Given the island routine used and the nature of these waves, groups of waves may not be directly connected even when they may be part of the same wave event. For example, the near- f_{ce} waves have harmonic structure. Often, both the harmonics and

the base frequency bands are above the 4 dB noise threshold, but the wave power between does not satisfy this condition. Therefore, the main band and harmonics are grouped as separate wave islands. A similar effect occurs when the wave power briefly ceases, then resumes. This is demonstrated by the left-most wave event on in Figure 2(d). Because the island routine groups only immediately adjacent pixels, a situation occasionally arises when two halves of a whole wave interval are grouped separately.

To mitigate this issue, after all filtering is applied, the remaining waves are regrouped. Separate wave intervals that occur less than 60 s apart are grouped together into a single interval. These start and end times are recorded into one final event list. This method also eliminates gaps in frequency, as waves that are separated only by a frequency gap necessarily occur less than 60 s from one another.

Quiescent regions are identified for the three orbit families of Encounters 1 through 6. Only regions with duration of 90 s or longer are considered. In total, 465 wave-active quiescent regions are identified, corresponding to a total time duration of 35.2 hr. The distribution of identified intervals by radial distance is as follows: seven regions occurred between 50 R_s and 45 R_s with a total duration time of 0.3 hr (0.9% of data), 31 regions occurred between 45 R_s and 40 R_s totaling 2.5 hr (7.1% of data), 210 regions between 40 R_s and 35 R_s totaling 13.8 hr (39.2% of data), 47 regions between 35 R_s and 30 R_s totaling 2.9 hr (8.2% of data), 160 regions between 30 R_s and 25 R_s totaling 15.3 hr (43.2% of data), and nine regions between 25 R_s and 20 R_s totaling 0.5 hr (1.4% of data).

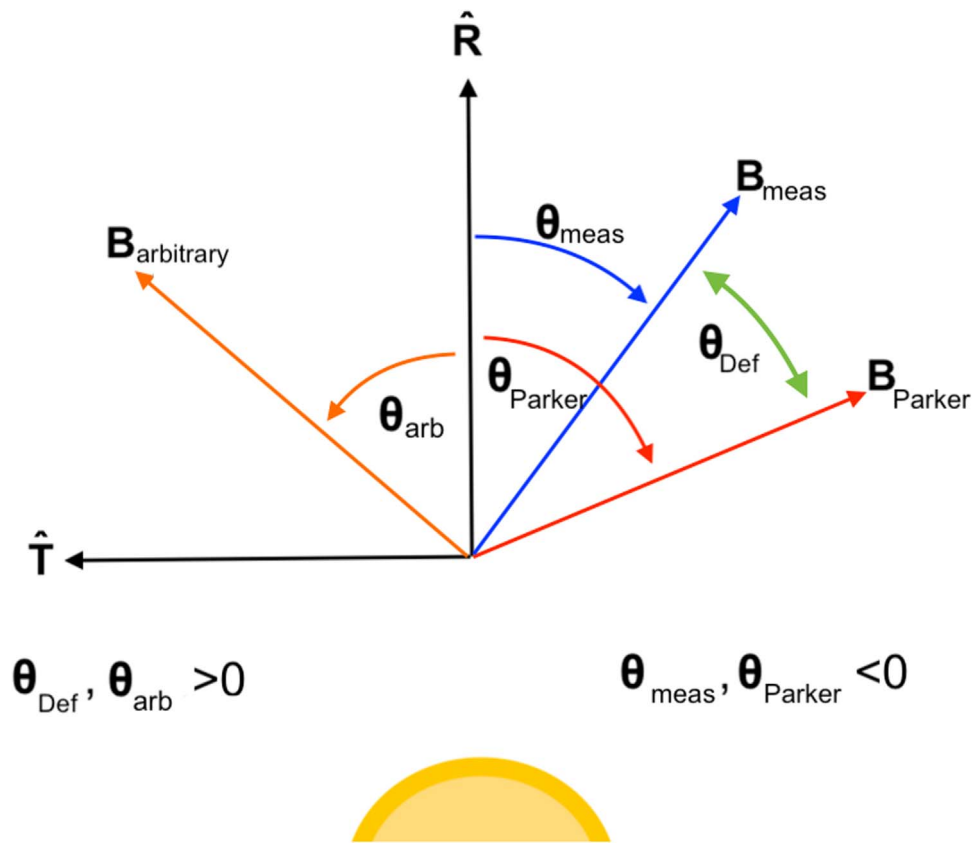


Figure 4. Cartoon depicting magnetic field angles relative to \hat{R} unit vector. $\hat{B}_{arbitrary}$ and θ_{arb} are arbitrary vectors and angles drawn to demonstrate angles in this coordinate system.

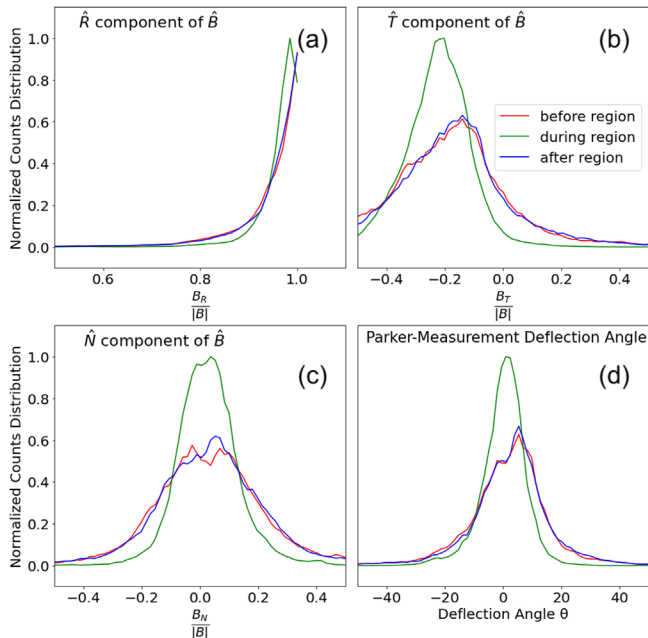


Figure 5. 1D Histograms constructed by integrating along the time axis of Figure 3. Figure 5(a) is the \hat{R} component of the unit vector. Figure 5(b) is the \hat{T} component. Figure 5(c) is the \hat{N} component. Figure 5(d) is the Parker deflection angle. SPC velocity values are used to calculate the Parker spiral for Encounter 1.

Once all regions are identified, a superposed epoch analysis is conducted on the plasma wave and solar wind properties of each wave-active quiescent region. Because each region spans

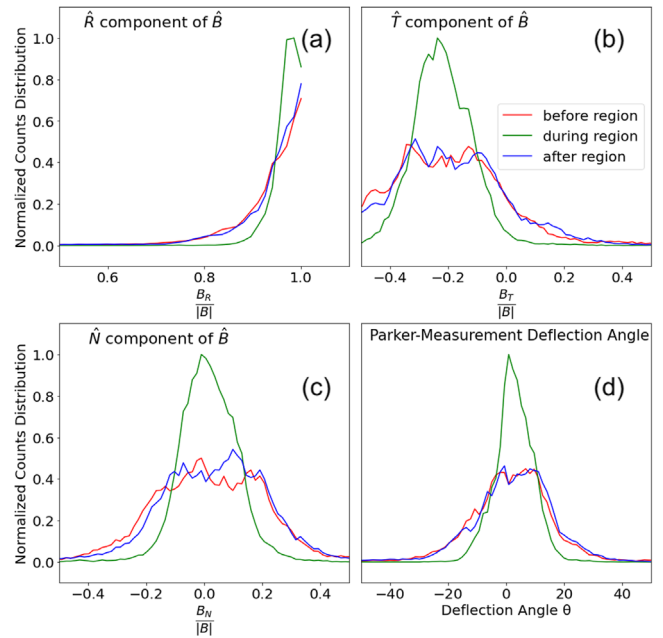


Figure 6. This figure is identical to Figure 5, with the exception that only Encounter 1 is included. Figure 6(a) is the \hat{R} component of the unit vector. Figure 6(b) is the \hat{T} component. Figure 6(c) is the \hat{N} component. Figure 6(d) is the deflection angle. SPC velocity values are used to calculate the Parker spiral for Encounter 1.

a different length of time, the data from all regions must be normalized in time. Before normalization, the number of data samples (N_o) for the shortest region is used to determine the

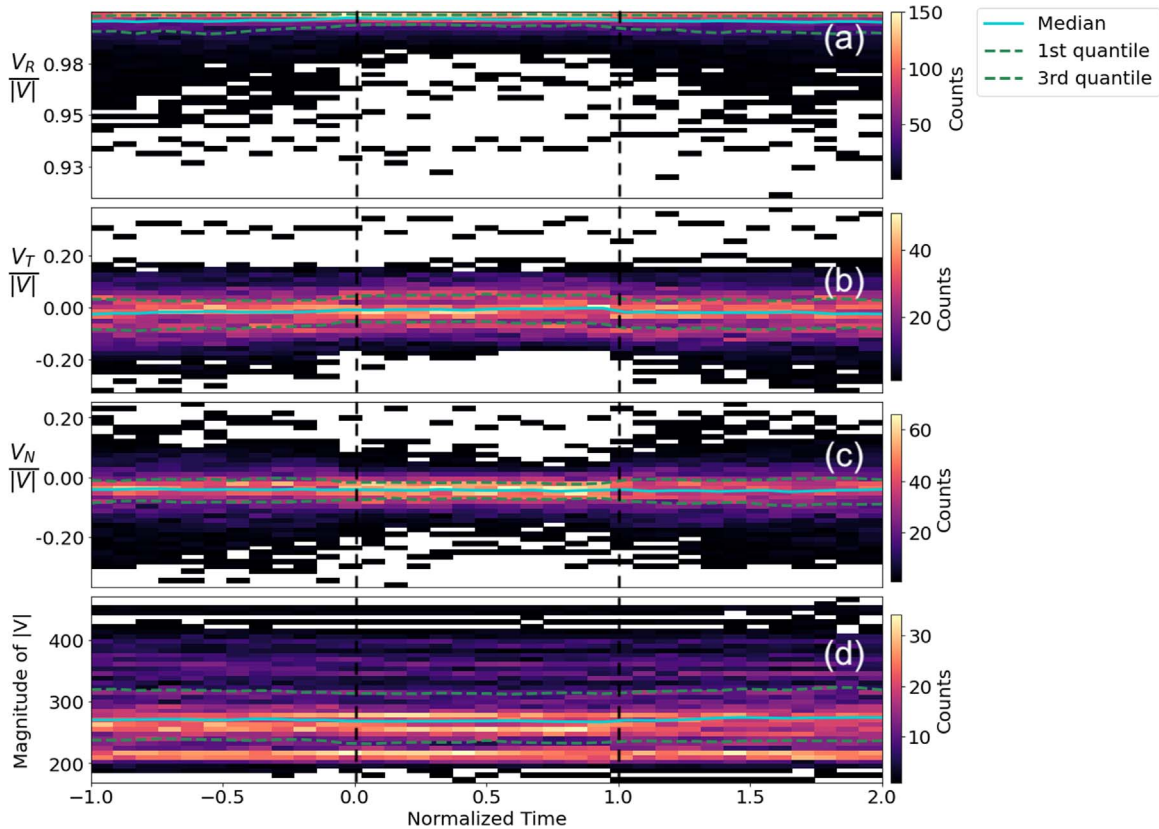


Figure 7. [Regions found for all radial distances. Excludes Encounter 1.] 2D histograms of RTN bulk velocity unit vectors and velocity magnitude. Figure 7(a) represents the \hat{R} component of the velocity unit vector in RTN coordinates. 7(b) is the \hat{T} component. Figure 7(c) is the \hat{N} component. Figure 7(d) is the magnitude of the solar wind velocity in km s^{-1} .

number of bins that data from all other regions should be divided into. After normalization, each region of data length $N > N_o$ is divided into N_o bins containing N/N_o data points. The median value of the examined quantity in each bin is assigned as the normalized value. In this way, the data from all time-normalized wave-active quiescent regions have length N_o . The total duration examined for each event is three times the event duration, to capture the behavior before, during, and after each wave-active quiescent region. The reason for this is that we are interested in the question of whether or not the waves demarcate a special region of plasma or a unique structure in the solar wind, and as such, we compare the regions to the plasma immediately neighboring them. There is no demand that the neighboring plasma be switchback or non-switchback regions.

The distance from PSP to the Sun changes significantly over an orbit, as do almost all solar wind ambient plasma quantities. To reduce the impact of radial variability on this analysis, the amplitude of examined quantities are normalized with radial distance. For example, the magnetic field vector components are normalized to the magnitude of the field vector, and the unit vector components are examined. Particle temperatures parallel and perpendicular to the background magnetic field are normalized to their median value across the normalization window, and temperature anisotropies are normalized by definition. Solar wind velocity is also normalized into a unit vector. Electron core drift did not change noticeably with radial distance and did not require any normalization. The width of the electron strahl distribution did change with radial distance, but the range of possible values for strahl width has a limited

range (0° to 180°), and radial variability was not sufficiently large to mask any trends.

3. Results

Figure 3 contains a 2D histogram of the ambient magnetic field unit vector components for all identified wave-active quiescent regions greater than 90 s in duration. Each interval has been normalized in time to the shortest time duration event, as described above. Figures 3(a), (b), and (c) show the magnetic field unit vector components in Radial, Tangential, Normal (RTN) heliocentric coordinates. Figure 3(d) shows the deflection angle from a theoretical Parker spiral (described below). Overplotted on each panel is the median value for each time bin (blue) and the first and third quartiles (dashed green). The data shown in this figure demonstrate a strong preference in direction for the unit vector components during the wave-active quiescent regions compared to the solar wind immediately adjacent to them. Moreover, there is a total absence of magnetic field switchbacks in these regions. PSP crosses the heliospheric current sheet multiple times (Szabo et al. 2020), and therefore, during some events the magnetic field is oriented sunward, whereas for other events, the field is oriented anti-sunward. For this superposed epoch analysis, the quantity \hat{B} is always defined to be anti-sunward, and the sign of \hat{B} is flipped when necessary.

The deflection angle from the theoretical Parker spiral to the magnetic field unit vector is calculated as follows. First, the theoretical Parker spiral deflection from radial θ_{Pa} was calculated using the rotation rate of the solar equatorial surface (ω),

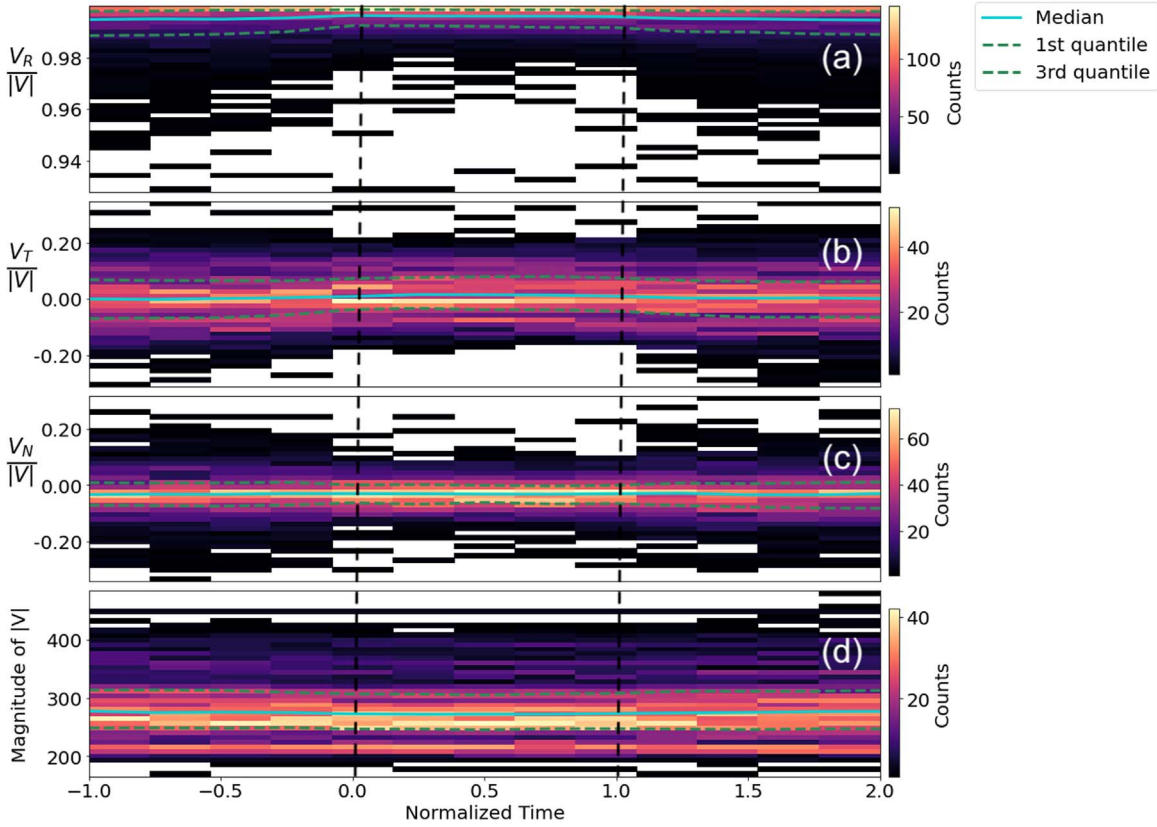


Figure 8. [Regions found at all R_s] 2D histograms of RTN bulk velocity unit vectors and velocity magnitude. Figure 8(a) represents the \hat{R} component of the velocity unit vector in RTN coordinates. 8(b) is the \hat{T} component. 8(c) is the \hat{N} component. Figure 8(d) is the magnitude of the solar wind velocity in km s^{-1} . SPC fits have been used to calculate the velocity for Encounter 1.

the distance of PSP from the solar surface (R), and the \hat{R} component of the solar wind proton bulk velocity vector as measured by SPAN-I:

$$\theta_{\text{Pa}} = \tan^{-1}(-\omega R_{\text{PSP}}/V_R). \quad (1)$$

Next, the angle of the measured magnetic field unit vector θ_{Meas} with respect to \hat{R} is calculated:

$$\theta_{\text{Meas}} = \tan^{-1}(B_T/B_R). \quad (2)$$

Finally, the deflection angle θ_{Def} is defined as the difference between these two angles:

$$\theta_{\text{Def}} = \theta_{\text{Meas}} - \theta_{\text{Pa}}. \quad (3)$$

In calculating these angles, Equations (1) and (2) always return negative numbers, so Equation (3) is equivalent to

$$\theta_{\text{Def}} = |\theta_{\text{Pa}}| - |\theta_{\text{Meas}}|.$$

Figure 4 depicts the described angles in a cartoon. With these definitions, $\theta_{\text{Def}} > 0$ corresponds to a more radial orientation of the magnetic field relative to a theoretical Parker spiral, while $\theta_{\text{Def}} < 0$ corresponds to more tangential orientation. $\mathbf{B}_{\text{arbitrary}}$ and the corresponding θ_{arb} are arbitrary vectors and angles used to demonstrate how angles relate to vectors in this coordinate system. As drawn, θ_{arb} and θ_{Def} are both positive while the angles θ_{meas} and θ_{Parker} are both negative.

The proton bulk velocity is measured at a significantly lower cadence than the magnetic field data. As a result, θ_{Parker} has lower resolution than $\theta_{\text{Measurement}}$. To rectify this, θ_{Parker} is interpolated to the cadence of $\theta_{\text{Measurement}}$.

Figure 5 shows data from Figure 3, integrated along the time axis. Each distribution pictured is normalized to its integrated area to facilitate comparison. Positive Parker deflection angles correspond to a more radial magnetic field orientation, and negative angles to more tangential orientations. From this analysis, it is found that the magnetic field unit vector is preferentially more radial before and after the wave-active quiescent intervals, compared to within the intervals. This behavior is consistent across all encounters except Encounter 1 (Figure 6). The deflection angle distributions before and after quiescent regions, with the exception of Encounter 1, are strongly peaked at about 7° toward the radial direction away from a theoretical Parker spiral. Encounter 1, in contrast, shows a plateau bounded by a $\pm 7^\circ$ deflection angle before and after the wave-active quiescent regions. An important detail to note is that the deflection angle of the measured magnetic field vector out of the RT plane was calculated and was found to be statistically isotropic about zero for quiescent regions and for regions before and after. This behavior is seen in the N component of the measured magnetic field in Figures 5 and 6, and it justifies restricting the deflection angle calculation to the RT plane.

Figure 7 is similar to Figure 3, but for bulk solar wind proton velocity. These data are strictly from SPAN-I and are measured at a much lower cadence than the magnetic field. The normalized intervals' lengths are the same as those used in the magnetic field analysis. The events included in Figure 7 are limited to those that occurred in Encounter 2 and beyond. This limitation is presented because the SPAN-I (SPC) measurement cadence during solar Encounter 1 was ~ 30 s (~ 20 s), whereas

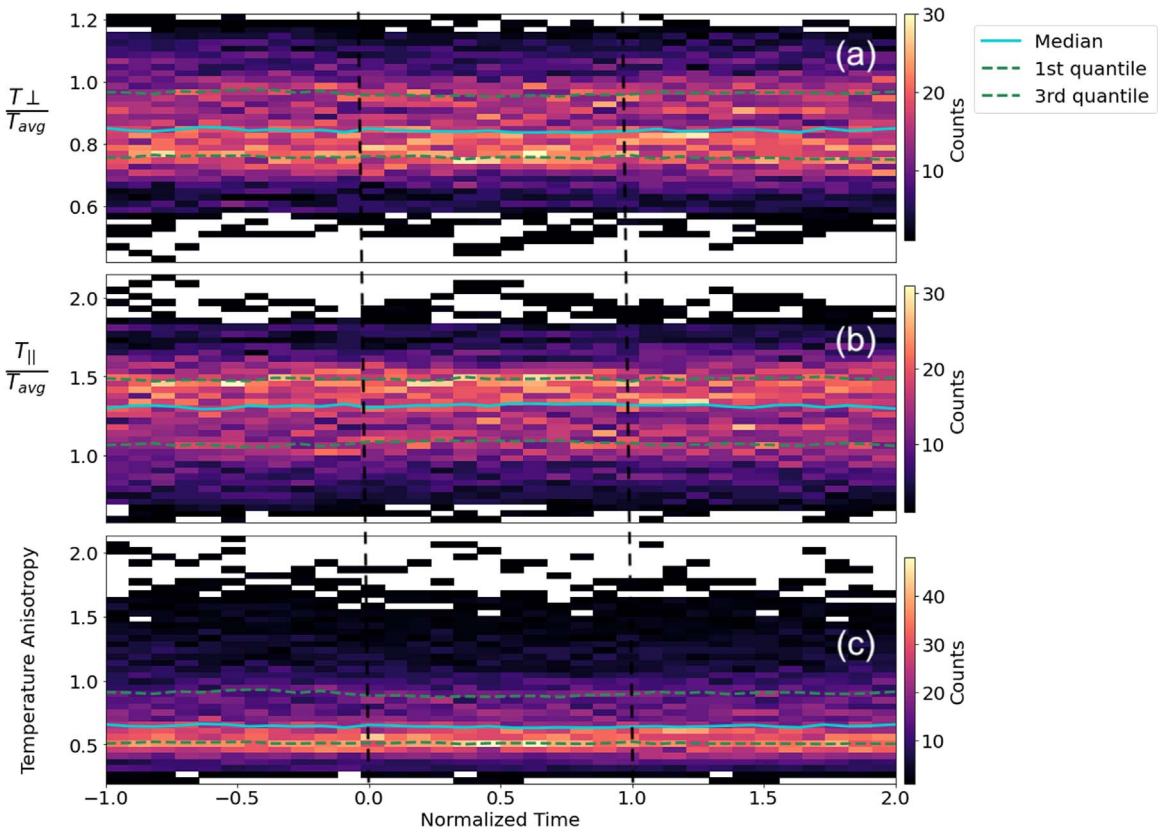


Figure 9. Histograms of proton temperature components and proton temperature anisotropy. Figure 9(a) is a 2D histogram over time of the component of the proton temperature perpendicular to the ambient magnetic field, normalized to the total temperature measured in the instrument frame. Figure 9(b) is the parallel component, also normalized to the total temperature. Figure 9(c) shows the temperature anisotropy.

it was higher on subsequent encounters. Encounter 1 had high quiescent region counts (105) but low time resolution. By excluding Encounter 1 data, higher time resolution is achieved in the superposed epoch analysis, but with lower statistics. When Encounter 1 data are included, variation appears in the velocity magnitude that does not appear in the high-resolution data, and it is not clear whether this effect is due to the inclusion of more events or an artifact of lower-resolution data.

From the data in Figure 7, the solar wind velocity shows a slight enhancement ($\sim 5 \text{ km s}^{-1}$) in the $+\hat{T}$ direction during the wave-active quiescent regions. While 5 km s^{-1} is within the SPAN-I instrument measurement margin of error (Kasper et al. 2016), it does appear systematically in these data, whether every quiescent region is considered or if only a subset of these regions are considered. Figure 8 is identical to Figure 7, except that data from all encounters are included. The velocity enhancement in the \hat{T} direction becomes more ambiguous.

Figure 9 shows the variation of proton temperature and its anisotropy inside and outside of wave-active quiescent regions. Here, proton temperature perpendicular and parallel to the background magnetic field are considered. There is no observed difference between the times before, during, and after the observed quiescent region.

Several electron distribution properties were also examined in this study. The width of strahl electron distribution, the temperature of the electron core distribution, the anisotropy of the core electron distribution, and the electron core sunward drift speed were all examined. All electron properties were determined using fits to the electron distributions measured by SPAN-e as in Halekas et al. (2020). Despite using near- f_{ce}

plasma waves, which are presumably electron-resonant, to identify quiescent regions, no clear variation was found in any of the examined electron distribution quantities before, during, and after the quiescent regions. However, it was found that the electron core sunward drift during the observed intervals was consistently higher than is typical across each encounter.

Figure 11 shows the distribution of electron core sunward drift for each solar encounter (blue) compared with the distribution of electron core sunward drift during wave-active quiescent regions for that encounter (orange). Encounter 3 is excluded because data on electron core drift are not available for that encounter. The distribution of electron core sunward drifts from near quiescent solar wind regions is consistently peaked at velocities higher than those of distributions from the entire encounter. Moreover, the distributions during regions are peaked roughly ~ 180 to $\sim 200 \text{ km s}^{-1}$, (with the exception of Encounter 6, which has low quiescent region statistics). This is consistent with the range of velocities that Malaspina et al. (2020) measured for electron core drift during near- f_{ce} wave events.

4. Discussion

4.1. Quiescent Regions and Near- f_{ce} Wave Growth

At least three definitions have been employed to identify regions of near-Sun solar wind characterized by low-amplitude magnetic turbulence. Dudok de Wit et al. (2020) measured the angle that ambient magnetic field makes with respect to a theoretical Parker spiral and associated quiescent regions with small off-Parker deflection angles. This method assumes that quiescent regions are associated with near-Parker spiral field configurations. Malaspina et al. (2020) examined the amplitude

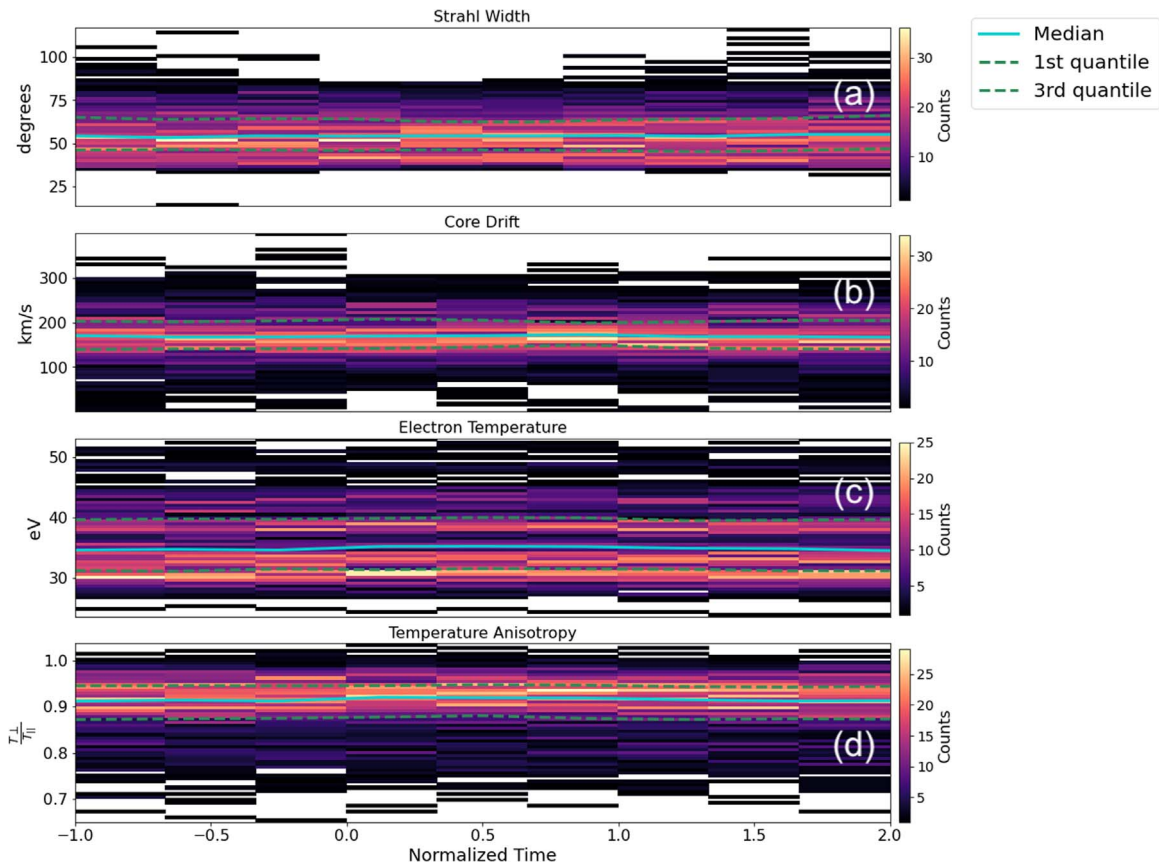


Figure 10. Superposed epoch analysis of electron properties inside and near wave-active quiescent regions. Figure 10(a) shows the measured component of the strahl width. Figure 10(b) shows the sunward drift of the thermal core electrons. Figure 10(c) shows the electron core temperature (average of parallel and perpendicular temperatures). Figure 10(d) shows the electron core temperature anisotropy.

of the magnetic field power spectral density at frequencies below 1 Hz. This method assumes nothing about the field configuration, but identifies quiescent regions based on an empirical magnetic fluctuation amplitude threshold value.

In this study, near- f_{ce} waves are used to identify quiescent regions that are wave-active. The use of these waves as markers eliminates the need for thresholds related to magnetic field fluctuations or angular deflections, but selects for properties of wave-active quiescent solar wind regions, which may not necessarily be the same as the properties of quiescent solar wind regions without wave activity.

One property for which this distinction is important is the electron core drift. The electron core drift is high during wave intervals, but does not noticeably change as the Parker Solar Probe enters and exits a wave-active quiescent region. Further, the identified waves are likely electron-resonant, because they are close to f_{ce} and appear in association with other electron-resonant waves such as electron Bernstein waves (Malaspina et al. 2021). The electron core drift is the only electron property identified that is systematically different between regions with and without wave growth. This behavior suggests that a higher sunward electron core drift speed is a necessary—but not sufficient—condition for the growth of the near- f_{ce} waves observed during wave-active intervals, and that it is a property of the plasma waves rather than the larger-scale quiescent region.

4.2. Quiescent Region Properties

Of the wave-active quiescent solar wind region properties examined, the most striking is the magnetic field data. The

magnetic field fluctuations in the identified wave-active quiescent regions are found to have low amplitudes relative to adjacent solar wind regions. Also, the solar wind bounding these quiescent regions shows preferential magnetic field orientations that are systematically more radial (by $\sim 7^\circ$ on average) compared to a theoretical Parker spiral. Locally measured solar wind velocity was used to determine the Parker spiral angle at each time, therefore this deflection is not due to the effect of changing wind speeds. So what is the origin of these quiescent region field geometries?

One possibility considered is that the solar wind that carries the quiescent solar wind region magnetic fields may originate relatively closer to the solar surface, compared to magnetic fields from adjacent solar wind plasma. If the quiescent region solar wind originated from lower in the solar atmosphere, perhaps the magnetic field lines would have had more time to spiral into the tangential direction relative to the neighboring solar wind. However, to explain a 7° deflection difference requires a launch height difference of $\sim 21 R_\odot$. This is unrealistic, given that PSP is located near $20 R_\odot$, when observing many quiescent regions. Further, there are minimal velocity changes observed between wave-active quiescent regions and the adjacent solar wind. If the quiescent region solar wind originated much lower than the solar wind in the regions before and after, then presumably these regions would acquire different solar wind speeds. Based on this reasoning, different launch heights cannot explain the observed solar wind magnetic field difference inside and out of wave-active quiescent regions.

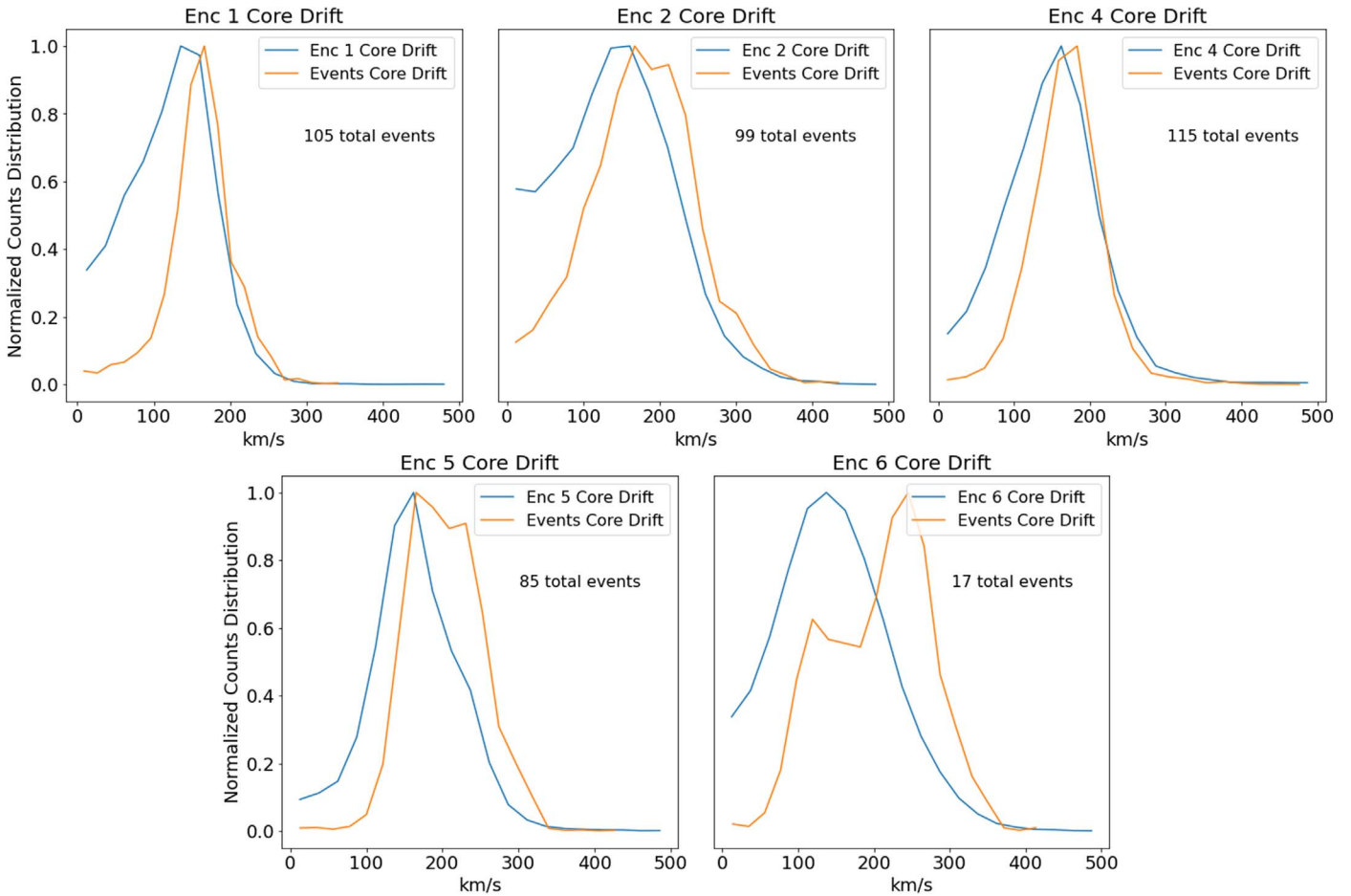


Figure 11. Distribution of electron core sunward drift values for each solar encounter (blue) and distribution of electron core sunward drift during wave-active quiescent regions identified within each encounter (orange).

Another possibility is that the wave-active quiescent regions are remnants of magnetic structure propagating radially outward from the solar corona. For example, if Parker Solar Probe’s trajectory cut through a flux rope at the correct angle, one could recover the observed Radial–Parker–Radial orientation of magnetic field lines near the quiescent regions. However, this only works if the Parker Solar Probe preferentially passes through flux ropes on the radially outward side (unlikely) or if the mechanism that generates the near- f_{ce} waves operates on only the radially outward side of flux ropes. Thus, the origins of quiescent regions remain the subject of ongoing research. This study does offer a constraint on possible solutions.

Another possible explanation is that the deflection in the magnetic field vector is related to a slight deflection in the velocity vector via local conservation of solar wind angular momentum. By equating the angular momentum flux from the protons to the magnetic field stresses, a change in tangential velocity may result in a tangential magnetic field deflection. The theoretical magnetic field deflection magnitudes expected based on angular momentum flux calculations matched the observed deflection for certain radial distances but not for others. The observed tangential velocity enhancement is found to be independent of radial distance, which might further suggest the deflection is due to some error rather than physical changes in the velocity vector.

Yet another explanation comes from potential growth mechanisms in the waves used to identify these regions. In the

work of Tigid et al. (2022), the authors demonstrate that the near- f_{ce} waves used as markers in this study require a more radial orientation of the field to be generated. This means that, by selecting the waves, we are demanding that the field have the peculiar orientation of being more radial statistically at either end of the event.

The proton bulk velocity vector and magnitude have little change across the boundaries of the wave-active quiescent regions. The median \hat{V}_T is observed to increase slightly. This increase is seen across individual encounters, including Encounter 4, which has high quiescent region statistics (115 quiescent regions). During these periods, the proton VDF was inspected and a majority of the core population of the VDF was captured in the SPAN-I FOV. In addition, the magnetic field does not highly vary during these regions. Highly variable magnetic fields comprise another source of error for interpreting partial plasma moments. This enhancement is $\sim 5 \text{ km s}^{-1}$ when expressed in absolute units, and is well within the error bars on the SPAN-I moment estimates, though it is worth noting that this \hat{V}_T deflection is systematic. The magnetic field geometry may be responsible for the observed slight changes. Within wave-active quiescent regions, the ambient magnetic field has a larger component in the \hat{T} direction compared to regions before and after, meaning that a slightly different portion of the proton distribution function (with respect to the ambient magnetic field direction) is visible to SPAN-I during wave-active quiescent regions. This could conceivably lead to a

systematic difference in the output of the proton core fitting routine.

The observed behavior of electrons through the wave-active quiescent regions was surprising. Because the regions were identified using seemingly electron-resonant plasma waves (near- f_{ce} waves), it was expected that electron distribution function properties would be different in the regions of wave growth compared to adjacent regions. Instead, little variation was observed across all electron distribution function quantities (Figure 10). While electron core sunward drift also shows little variation between wave-active quiescent regions and the adjacent solar wind, core drift is found to be consistently high ($\sim 175 \text{ km s}^{-1}$ sunward) near wave-active regions when compared to full-encounter statistics, as demonstrated by Figure 11. This is consistent with what is measured in Malaspina et al. (2020), and may suggest that the core drift and/or the associated strahl electrons are a necessary—but not sufficient—condition for the generation of the near- f_{ce} waves.

The proton core temperatures and anisotropies, as calculated with using the SPAN-I moments, do not appear to change between the quiescent intervals and the neighboring plasma regions. Comparing this to previous studies of switchbacks and switchback patches, Woolley et al. (2020) found, using SPC, that the proton temperature parallel ($T_{p,\parallel}$) to the background field did not vary between individual switchbacks and their surrounding plasma. Bale et al. (2021), using SPAN-I, observe variability between patches of switchbacks and surrounding plasma, finding that both the proton temperature perpendicular ($T_{p,\perp}$) and proton temperature parallel ($T_{p,\parallel}$) are enhanced within switchback patches. In contrast to both of these, Woodham et al. (2021), using SPAN-I, find that there are $T_{p,\parallel}$ enhancements present in both individual switchbacks as well as switchback patches. The complex interaction between the SPAN-I and SPC fields of view and the measured plasma environment make accurate determination of this quantity difficult. Further, in Bale et al. (2021), a velocity enhancement is observed at the same time as the $T_{p,\perp}$ enhancement, whereas Woodham et al. (2021) did not observe either, so it is possible that, if the velocity enhancement is tied to the $T_{p,\perp}$ enhancement, these studies are not inconsistent.

This study focused on regions with minimal magnetic variation, and determined that the proton temperature distribution does not vary systematically between quiescent and quiescent-adjacent regions. It is possible that, because this study examines only individual quiescent patches, variability on other scale sizes may be present. For example, Bale et al. (2021) and Woolley et al. (2020) found temperature variability between switchback patches (which last on the order of hours) but not between individual switchbacks. Likewise, it is possible that the wave-active quiescent regions (on the order of minutes) examined in this study are not different enough from their immediate surroundings to have noticeable changes in the temperature distribution. This is currently speculative and warrants further study. It is also possible, however, that Woodham et al. (2021) is the correct analysis and that switchbacks and switchback patches present enhancements in $T_{p,\parallel}$. Assuming that these wave-active quiescent regions represent the regions between switchback patches as in Dudok de Wit et al. (2020), we would expect to observe a $T_{p,\parallel}$ decrease when moving from non-quiescent intervals to quiescent intervals. Yet this is not observed in this analysis. This may be a reflection of the fact that these wave-active quiescent

regions are small-scale (2 to 5 minutes in duration) compared to those found in Dudok de Wit et al. (2020), making them not easily differentiable from the surrounding, potentially still quiescent, plasma. It also could be suggest that these wave-active regions are unique plasma structures altogether.

5. Conclusion

In this paper, we presented observations and analysis of quiescent regions in the solar wind. Quiescent regions display exceptionally low-amplitude magnetic field fluctuations and host various plasma waves, including near- f_{ce} plasma waves, which are observed exclusively in quiescent regions. It is shown that the quiescent regions contain minimal magnetic field variation and are entirely devoid of magnetic switchbacks. In quiescent solar wind regions, the magnetic field vector closely follows the theoretical Parker spiral, while regions just outside prefer more radial orientations. Despite displaying significant changes in the behavior of the magnetic field vector during quiescent regions, plasma particle properties are, to first order, uniform between the quiescent regions and their neighboring regions. These results should enable further investigation into how significant a role switchbacks and magnetic field turbulence play in the heating of solar wind plasma. Future studies will examine how the magnetic properties of quiescent solar wind regions may be linked to the solar origins of these regions.

Parker Solar Probe was designed, built, and is now operated by the Johns Hopkins Applied Physics Laboratory as part of NASA's Living with a Star (LWS) program (contract NNN06AA01C). Support from the LWS management and technical team has played a critical role in the success of the Parker Solar Probe mission.

A.J.F. is funded by the European Research Council (ERC) under the European Union's Horizon 2020 research and innovation program (grant agreement No 810218 WHOLESUN).

Data manipulation was performed using the Numpy (Harris et al. 2020) and Scipy (Virtanen et al. 2020) Python packages. Figures in this work were produced using the Python package Matplotlib (Hunter 2007).

ORCID iDs

Benjamin Short  <https://orcid.org/0000-0003-3945-6577>
 David M. Malaspina  <https://orcid.org/0000-0003-1191-1558>
 Jasper Halekas  <https://orcid.org/0000-0001-5258-6128>
 Orlando Romeo  <https://orcid.org/0000-0002-4559-2199>
 J. L. Verniero  <https://orcid.org/0000-0003-1138-652X>
 Adam J. Finley  <https://orcid.org/0000-0002-3020-9409>
 Justin C. Kasper  <https://orcid.org/0000-0002-7077-930X>
 Ali Rahmati  <https://orcid.org/0000-0003-0519-6498>
 Stuart D. Bale  <https://orcid.org/0000-0002-1989-3596>
 John W. Bonnell  <https://orcid.org/0000-0002-0675-7907>
 Anthony W. Case  <https://orcid.org/0000-0002-3520-4041>
 Thierry Dudok de Wit  <https://orcid.org/0000-0002-4401-0943>
 Keith Goetz  <https://orcid.org/0000-0003-0420-3633>
 Katherine Goodrich  <https://orcid.org/0000-0002-4288-5084>
 Peter R. Harvey  <https://orcid.org/0000-0002-6938-0166>
 Kelly E. Korreck  <https://orcid.org/0000-0001-6095-2490>
 Davin Larson  <https://orcid.org/0000-0001-5030-6030>
 Roberto Livi  <https://orcid.org/0000-0002-0396-0547>
 Robert J. MacDowall  <https://orcid.org/0000-0003-3112-4201>
 Marc Pulupa  <https://orcid.org/0000-0002-1573-7457>

Michael L. Stevens  <https://orcid.org/0000-0002-7728-0085>
 Phyllis Whittlesey  <https://orcid.org/0000-0002-7287-5098>

References

- Axford, W. I., McKenzie, J. F., Sukhorukova, G. V., et al. 1999, *SSRv*, **87**, 25
- Bale, S. D., Badman, S. T., Bonnell, J. W., et al. 2019, *Natur*, **576**, 237
- Bale, S. D., Goetz, K., Harvey, P. R., et al. 2016, *SSRv*, **204**, 49
- Bale, S. D., Horbury, T. S., Velli, M., et al. 2021, *ApJ*, **923**, 174
- Bruno, R., & Carbone, V. 2013, *LRSP*, **10**, 2
- Chandran, B. D. G., Li, B., Rogers, B. N., Quataert, E., & Germaschewski, K. 2010, *ApJ*, **720**, 503
- Drake, J. F., Agapitov, O., Swisdak, M., et al. 2021, *A&A*, **650**, A2
- Dudok de Wit, T., Krasnoselskikh, V. V., Bale, S. D., et al. 2020, *ApJS*, **246**, 39
- Fargette, N., Lavraud, B., Rouillard, A. P., et al. 2021, *ApJ*, **919**, 96
- Halekas, J. S., Whittlesey, P., Larson, D. E., et al. 2020, *ApJS*, **246**, 22
- Harris, C. R., Millman, K. J., van der Walt, S. J., et al. 2020, *Natur*, **585**, 357
- Horbury, T. S., Woolley, T., Laker, R., et al. 2020, *ApJS*, **246**, 45
- Hunter, J. D. 2007, *CSE*, **9**, 90
- Kasper, J. C., Abiad, R., Austin, G., et al. 2016, *SSRv*, **204**, 131
- Kasper, J. C., Bale, S. D., Belcher, J. W., et al. 2019, *Natur*, **576**, 228
- Livi, R., Larson, D. E., Kasper, J. C., et al. 2021, *ESSOAr*, **1**, 20
- Malaspina, D. M., Ergun, R. E., Bolton, M., et al. 2016, *JGRA*, **121**, 5088
- Malaspina, D. M., Halekas, J., Bercic, L., et al. 2020, *ApJS*, **246**, 21
- Malaspina, D. M., Wilson, L. B. I., Ergun, R. E., et al. 2021, *A&A*, **650**, A97
- Matteini, L., Stansby, D., Horbury, T. S., & Chen, C. H. K. 2018, *ApJL*, **869**, L32
- Mozer, F. S., Bonnell, J. W., Bowen, T. A., Schumm, G., & Vasko, I. Y. 2020, *ApJ*, **901**, 107
- Porsche, H. 1981, in ESA Special Publication, Solar System and its Exploration, ed. W. R. Burke, Vol. 164 (Paris: ESA), 43
- Schwadron, N. A., & McComas, D. J. 2021, *ApJ*, **909**, 95
- Shoda, M., Chandran, B. D. G., & Cranmer, S. R. 2021, *ApJ*, **915**, 52
- Squire, J., Chandran, B. D. G., & Meyrand, R. 2020, *ApJL*, **891**, L2
- Szabo, A., Larson, D., Whittlesey, P., et al. 2020, *ApJS*, **246**, 47
- Tigik, S. F., Vaivads, A., Malaspina, D. M., & Bale, S. D. 2022, *ApJ*, **936**, 7
- Virtanen, P., Gommers, R., Oliphant, T. E., et al. 2020, *NatMe*, **17**, 261
- Whittlesey, P. L., Larson, D. E., Kasper, J. C., et al. 2020, *ApJS*, **246**, 74
- Woodham, L. D., Horbury, T. S., Matteini, L., et al. 2021, *A&A*, **650**, L1
- Woolley, T., Matteini, L., Horbury, T. S., et al. 2020, *MNRAS*, **498**, 5524